Taylor & Francis
Taylor & Francis Group

Check for updates

Ultrafast optically induced resonant and non-resonant current generation in atoms and nanostructures: role of the photons orbital angular momentum

J. Wätzel[a], I. Barth[b] and J. Berakdar[a]

[a]Institute for Physics, Martin-Luther-University Halle-Wittenberg, Halle, Germany; [b]Max Planck Institute of Microstructure Physics, Halle, Germany

ABSTRACT

Aside from technological applications, steering non-equilibrium currents in electronic matter delivers information on the system electric and magnetic properties and their relation to electronic correlation and the underlying symmetry of the electrons' confinement. This theoretical study demonstrates that optical vortices are a versatile tool for spatio-temporal generation of charge currents via resonant and stimulated Raman-type processes for semi-conductor-based nanostructures as well as for atoms, thereby the orbital angular momentum associated with the optical vortex plays a key role.

1. Introduction

The orbital and spin parts of the angular momentum of electromagnetic waves were analysed and described theoretically long ago (cf. e.g. (1–4)). The relatively recent revival of this topic is fuelled by the astonishing advances in producing and tailoring light waves carrying orbital angular momentum (OAM) (5–11) in wide laser parameter range. Such waves with their helical wave front circling around the propagation direction are also called optical vortices. Substantial research efforts are currently devoted to exploiting the OAM-light–matter interactions with various prospect, and already demonstrated applications ranging from optical tweezers for microscale objects to electronics and life sciences, quantum information, astronomy or optical telecommunications (12–24). Notably, OAM beams extend the range of the mechanical action of light with such effects as moving, trapping and rotating microscopic objects (25–27), atoms, molecules (28–30), and Bose–Einstein condensates (31) as well as a charge distribution. The latter is the topic of this paper.

Inducing resonantly intraband transitions in a semi-conductor-based nanostructures via OAM laser pulses was shown to trigger orbital unidirectional current with a magnitude set by the so-called topology charge ℓ_{OAM} of the vortex, i.e. the quantity that quantifies the winding number of the wave front around the average wave vector in one optical wave length. Taking the spin-orbit interaction into account, e.g. Rashba-type spin-orbital coupling, spin-dependent currents can be manipulated optically (32–34) making OAM-carrying lasers ideal for

optical-based spintronics. Recently, these theory predictions were qualitatively evidenced by a recent experiment (35). Also for the magnetization control via light, so-called optomagnetism (36), OAM-carrying pulses are useful. In fact, we showed recently that below-band gap OAM-carrying laser pulses acting on a ferromagnetic insulator generate via stimulated Raman scattering femtosecond magnetic field bursts (37) that are capable of triggering an ultrafast transversal magnetization dynamics. Optical vortices (37) may offer some advantages over conventional optical switching (36) as the effective fields acting on the magnetization may be increased by increasing ℓ_{OAM}, but perhaps more importantly much more localized induced field might be achieved by combining optical vortices making this scheme attractive for nano-magnetism (spatial resolution of conventional optical switching (36) is set by the Abbe limit).

Generally, non-resonant Raman-type processes involve much less Joule heating than absorptive (resonance) processes. We expect this advantage to go on the cost of lower currents. In addition, as a second-order process in the field, the non-resonant process requires however high intensities entailing the need for short, few cycle pulses to avoid material damage. Yet another aspect which is important for technological applications is that, while the frequency has to be non-resonant, the optical period has to be much smaller than the carrier effective life time due to defects scattering. This condition is important to avoid collisional-assisted photoabsorption leading to energy dissipation and coherence loss. Here we

---

TH-2017-47

will study and compare non-resonantly and resonantly generated orbital current in nanoscale objects down to atoms.

For atomic size orbitals, the vast difference between the OAM-carrying beam waist and the orbital extension is an obstacle (38) for an efficient transfer of OAM. Nonetheless, using clusters such as fullerenes and magnetic endohedrals one can generate sizable currents via resonant fields (for instance, an ultraviolet vortex femtosecond pulse with an intensity of $\approx 10^{13}$ W/cm^2 generates in C_{60} a non-invasive nA unidirectional surface current with an associated magnetic field of hundreds mT at the centre of the fullerene (39)).

2. Non-resonant photovoltaic effect of the quantum ring

Let us consider at first a mesoscopic phase-coherent GaAs-AlGaAs-based ring (such as that realized experimentally in Refs. (40, 41)) irradiated by OAM-carrying electromagnetic pulses causing intra conduction band transitions. In the resonant case, we have shown (32, 33) that the light–matter interaction leads to a centrifugal drift flow of carriers and hence to a time-sustainable carriers accumulation at the ring outer boundary. The drift current generation is related to the exchange of OAM between the light and the carriers and is not related to the media noncentrosymmetric crystal structure (42, 43) (as conventionally needed for photogalvanic and bulk photovoltaic effect occurring for example in doped lithium niobate or bismuth ferrite). Hence, the present effect is much more general and is also expected to appear for stimulated Raman-type processes. Details on the theoretical description of the static properties of the investigated quantum rings are detailed in (33). Experimentally, the carrier density (and hence the Fermi level) as well as the geometric parameters of the ring are experimentally tunable in a wide range. We are interested in a nanosize quantum ring with the Fermi energy chosen as $E_F = 75$ meV. The ring is irradiated by a vortex beam focussed on the ring structure which has an average radius of $r_0 = 50$ nm. The corresponding band structure of the electron states characterized by the collective quantum number α (which refers here to the radial quantum number n_0 and the angular quantum number m_0) is shown in Figure 1(a). So, the initial situation is comparable to Figure 3(b) in Ref. (33). In the resonant case, we considered a photon energy $\hbar\omega = 5$ meV leading to resonant transitions from the first to the second radial band. In contrast, we use here a photon energy of $\hbar\omega = 4$ meV, i.e. only non-resonant transitions around the Fermi energy for the considered ring structure can be initiated due to the interaction with the OAM pulse (cf. the energy spectrum

in Figure 1(a)). The peak intensity is relatively moderate $I = 10^{10}$ W/cm^2. However, the frequency is very small, making a perturbation approach (at least to a second order to capture the stimulated Raman processes) unsuitable.

The interaction Hamiltonian which enters the two-dimensional time-dependent Schrödinger equation (2D-TDSE) is given by

$$\hat{H}_{\text{int}} = \frac{1}{2}\left[\hat{\boldsymbol{p}}\cdot\boldsymbol{A}(\boldsymbol{r},t) + \boldsymbol{A}(\boldsymbol{r},t)\cdot\hat{\boldsymbol{p}}\right]. \quad (1)$$

We assume a gauge where the scalar potential vanishes. The vector potential of the applied OAM beam reads

$$\boldsymbol{A}(\boldsymbol{r},t) = \Re\left\{\hat{\epsilon}A_0 f_{\ell_{\text{OAM}}}^q(\boldsymbol{r})e^{i\ell_{\text{OAM}}\varphi}\Omega(t)e^{i\omega t}\right\} \quad (2)$$

where the temporal profile is described by $\Omega(t) = \sin^2(\pi t/\tau_s)$ and the polarization state is $\hat{\epsilon}$. The radial profile of the optical vortex beam is described by Gaussian–Laguerre modes:

$$f_{\ell_{\text{OAM}}}^q(\boldsymbol{r}) = e^{-\frac{r^2}{w_0^2}}\left(\frac{\sqrt{2}r}{w_0}\right)^{|\ell_{\text{OAM}}|}L_q^{|\ell_{\text{OAM}}|}\left(\frac{2r^2}{w_0^2}\right). \quad (3)$$

The vector $\boldsymbol{r}$ is in the x/y-plane. The functions $f_{\ell_{\text{OAM}}}^q(\boldsymbol{r})$ are further determined by the waist size w_0 and the radial index q while $L_q^{|\ell_{\text{OAM}}|}\left(\frac{2r^2}{w_0^2}\right)$ are the Laguerre polynomials. For $q = 0$, $|\boldsymbol{A}(\boldsymbol{r},t)|^2$ has a donut shape. The 2D-TDSE is solved fully numerically for all carrier states with a real time propagation method. Therefore, the vortex field is accounted for to all orders (within the accuracy of the numerics).

To provide a qualitative comparison with the case where the class of resonant electronic transitions dominate the generation of the photocurrent, we consider the quantum ring structure wired with a 35 nm wide conductive straight bar. Note that the modification of the potential destroys the angular symmetry of the system with respect to the centre of the ring. Therefore, the description of the electron states via the radial quantum number n_0 and the angular quantum number m_0 is not possible anymore. The whole modification of the potential landscape is described in more details in Ref. (33).

The interaction of the OAM light with the ring structure leads to an effective increase of the centrifugal potential which causes a tunneling of the charge carriers into the wire. This mechanism is nicely demonstrated in Figure 1(b) by the time-dependent density of the occupied states (tDOS) after the interaction with a two-cycle OAM pulse amounting to a pulse duration of $\tau_s = 2.06$ ps. It can be calculated as
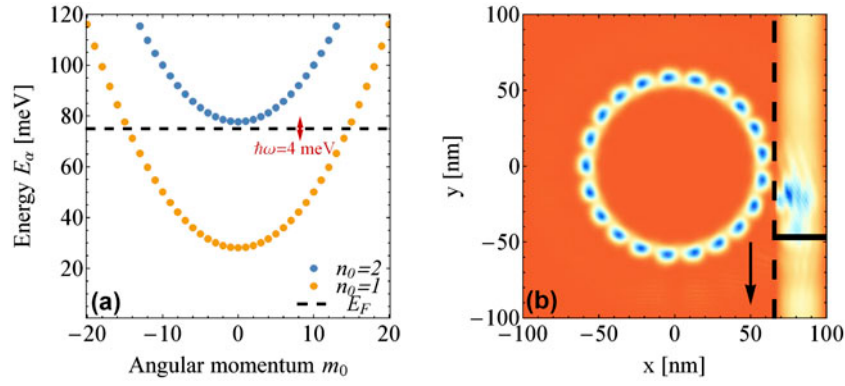
Figure 1. Wheel structure (bright area in (b)) consisting of quantum ring from which carriers are photo-pumped into a conductive channel leading to a directed charge current. (a) The band structure of the ring system used for the investigation of the non-resonant photovoltaic effect. The OAM-carrying laser is focused on the ring area and impinges perpendicular to the plane of the ring. The photon energy is $\hbar\omega = 4$ meV (not drawn to scale) which is too small to initiate resonant particle–hole transitions around the Fermi energy. The collective quantum number α of the individual electron states refers here to the radial quantum number n_0 and the angular quantum number m_0. (b) The tDOS $\rho^{\text{tDOS}}(t)$ of the studied ring-structure with an attached wire just after the application of the pulse at a propagation time of 2 ps. Upon irradiation the initially homogeneous tDOS exhibits 21 nodal structures reflecting the topological charge $\ell_{\text{OAM}} = -20$ and the helicity of -1 of the applied circularly polarized OAM beam.

$$\rho^{\text{tDOS}}(x, y, t) = \sum_{\alpha} f_\alpha(t) |\Psi_\alpha(x, y, t)|^2, \qquad (4)$$

where $\Psi_\alpha(x, y, t)$ are the wave functions of the electronic states characterized by the collective quantum number α and the energy eigenvalues E_α. The weights $f_\alpha(t)$ are the non-equilibrium distribution functions obtained from the Boltzmann equation with the relaxation time approximation (33, 44, 45). Within this approximation, all relaxation processes are introduced by means of the averaged relaxation time τ_{rel}. In the static case ($t = 0$), the weights are given by the equilibrium distribution functions $f_\alpha^0(E_f) = 1/\left[1 + \exp\left((E_\alpha - E_f)/k_B T\right)\right]$ where T is the temperature and k_B is the Boltzmann constant. For a temperature $T \to 0$ they behave like a Heaviside Theta function, i.e. in the static case $\rho^{\text{tDOS}}(x, y, t = 0) = \sum_{\alpha} \Theta(E_F - E_\alpha) |\Psi_\alpha(x, y, t)|^2$. Throughout the whole considerations, a relaxation time $\tau_{\text{rel}} = 25$ ps is assumed.

A direct consequence of the tunneling is a directed flow of the current density in the wire. In Figure 2 the corresponding photo-induced currents through a detector (marked by the thick horizontal line in Figure 1(b)) in the wire are depicted. The results of Ref. (33) which are an effect of resonant electron transitions are also included for a qualitative comparison. Two main features are salient. First, the photovoltaic effect is induced by non-resonant transitions, which might be expected for second order processes. It is important to emphasize that the current of interest here is the *unidirectional* current $I(t)$, which is already averaged over the fast oscillations. The time dependence of $I(t)$ is related to the population decay (46). Hence, the dynamics of this decay proceeds

irrespective of how these states were populated (by resonant or non-resonant transitions). Usually, the dynamics of $I(t)$, which belongs to the realm of quantum kinetics, can be dealt with either by a density-matrix truncation scheme (46), the non-equilibrium Greens function approach (47), or other methods (the classical Boltzmann equation might be considered however at short times its use is questionable (47)). Here we make use of the fact, that we only induce transitions around the Fermi levels (as we inferred by analysing which states are populated upon the pulse) and our system is weakly interacting, hence one may apply the relaxation time approximation (33, 48) or a particle conserving version of it, as done in Ref. (49). By doing so, the photocurrent is a summation of partial currents carried by the transient single-particle states $\Psi_\alpha(x, y, t)$ as deduced from the time evolution dictated by the 2D-TDSE, i.e.

$$I(t) = \sum_{\alpha} f_\alpha(t) I_\alpha(t), \qquad (5)$$

where $f_\alpha(t)$ is the non-equilibrium distribution function calculated with the relaxation time approximation (33) and $I_\alpha(t)$ are the individual contributions of the electron states characterized by α to the total current. Analysing the involved states shows that in the case of non-resonant transitions only the two excited states around the Fermi energy are current-carrying while in the case of the resonant transitions in Ref. (33) many more states deliver contributions to the total current. Nevertheless, the photo-induced currents in both cases are of the same magnitude.
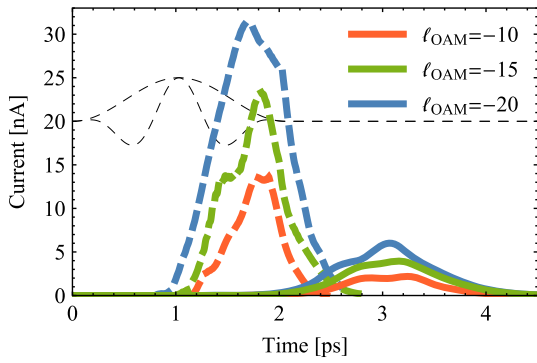
Figure 2. The photo-induced currents for a two cycle pulse (pulse duration $\tau_s = 2.06$ ps) with a non-resonant photon energy of $\hbar\omega = 4$ meV (solid lines) in comparison to the results discussed in Ref. (*33*) (dashed lines). The used intensity is 10^{10} W/cm^2 in both cases. The black dashed lines show the temporal variation of the applied OAM laser beam.

Figure 3. The photo-induced currents for different intensities and pulse durations of the employed optical vortex pulse. The non-resonant photon energy is $\hbar\omega = 4$ meV and the topological charge amounts to $\ell_{OAM} = -10$. The dashed lines show the corresponding temporal variations of the applied OAM laser beams with different durations and intensities.

Another interesting aspect is that the photo-induced currents increase much later in time. The time lag in the current buildup in the case of stimulated Raman processes can be understood if we consider the short-time population dynamics, as follows from a short-time expansion of the Dyson equation for the propagator. Let us consider qualitatively the dynamics on the time scale of the onset time of the pulse. No matter how short this pulse is it has to start weak and smooth, in which case perturbation theory gives a reasonable insight into this regime. As established for first-order (resonant) processes the population increases quadratically in time. For purely non-resonant transitions the population increases fastest with t^4. This dynamical behaviour in the case of a weak field follows the time-dependence of the population buildup as dictated by the first and the second-order time-dependent perturbation theory. The corresponding time structure is reflected in the unidirectional current, as the latter is mainly associated with the population dynamics (*46*). This short time hierarchy may be useful to distinguish between the processes in question. It reveals however some complications with the stimulated Raman excitations in the way it is treated here, when the current buildup time becomes comparable with the relaxation time due to scattering from phonons or vibrons and hence the adiabatic decoupling need to be reconsidered. Hence, a detailed study for instance along the lines of Ref. (*46*) might be useful but to our knowledge has not been conducted yet. As evidenced by Figure 2, one may state that the current and the photovoltaic effect can be enhanced effectively by increasing the topological charge of the optical vortex which leads to an enlarged transfer of OAM to the charge carriers which is accompanied by a larger centrifugal force. By photovoltaic effect we mean here the internal voltage buildup counteracting the

charge imbalance that builds up between the inner and outer boundaries of the ring.

In Figure 3 we show the time-resolved dependence of the photo-induced currents on the pulse parameters for a topological charge $\ell_{OAM} = -10$ of the optical vortex pulse. The red solid curve is the current corresponding to Figure 2 which was obtained by employing an OAM laser pulse with an intensity of 10^{10} W/cm^2, and a pulse duration of $\tau_s = 2.06$ ps. The green curve shows the current for the same intensity and a duration which is twice as long, i.e. $\tau_s = 4.12$ ps (four optical cycles). The purpose is to have an insight into the Floquet regime (longer pulses were unfortunately hammered by numerical limitations for longer propagation times). The consequence is a larger FWHM but also a longer build-up time of the current peak. Therefore, the temporal profile of the pulse which is characterized by $\sin[\pi t/\tau_s]^2$ is mapped into the photo-induced current which emphasizes the dependence of the magnitude of the photovoltaic effect on the intensity of laser beam. Although the intensity is equal in both cases, the maximum of the longer pulse is slightly smaller which can be explained by the set in of relaxation processes (relaxation time $\tau_{rel} = 25$ ps).

The blue, dashed curve corresponds to an intensity of 5×10^{10} W/cm^2 at a pulse duration of $\tau_s = 2.06$ ps (two optical cycles). The curve reveals that the maximum of the photo-induced current with a higher intensity is larger. This observation is explainable by the short time expansion of the propagator mentioned above and the population decay time τ_{rel} (in our case $\tau_{rel} = 25$ ps). The intensity at the respective short times enters as a prefactor for the time dependence of the population generation. This prefactor is smaller for longer pulses and larger for stronger pulses with the same duration. Inspecting the time dependent polarization is not only important
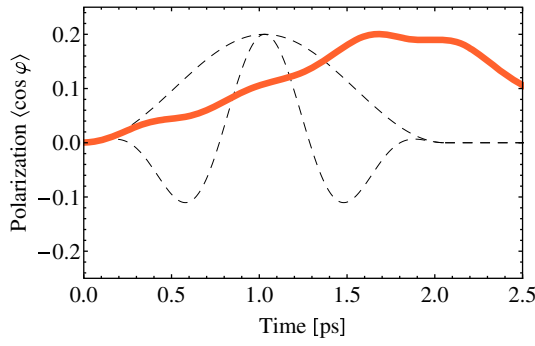
Figure 4. Time dependent polarization parameter $\langle \cos \varphi \rangle$ for a non-resonant photon energy of $\hbar\omega = 4$ meV, a pulse duration of $\tau_s = 2.06$ ps, an intensity of 10^{10} W/cm^2 and a topological charge of $\ell_{OAM} = -10$ of the vortex beam. The black-dashed lines show the temporal profile of the applied OAM pulse.

to complement the above analysis but it also delivers insight into the emission characteristics. We consider the polarization along the x axis (cf. Figure 1). The key quantity is then

$$\langle \cos \varphi \rangle (t) = \sum_\alpha f_\alpha(t) \int dx \int dy \, |\Psi_\alpha(x,y,t)|^2 \cos \varphi,$$

(6)

where $\varphi(x,y) = \arctan(x,y)$ is the polar angle with respect to the centre of the ring structure. The integration domain is restricted to the quantum ring meaning $x \leq 60$ nm. In molecular physics, this parameter is used for characterization of the polarization orientation of polar molecules (45, 50–52). It varies in the interval $[-1, 1]$ where the extremes mean the perfect orientation at the angles $\varphi = \pi$ or $\varphi = 0$ (along the x axis). Note that $\langle \cos \varphi \rangle (t) = 0$ does not necessarily mean that the object is orientated at the angles $\varphi = \pi/2$ or $\varphi = 3\pi/2$, but rather the density of states is distributed symmetrically with respect to the y-axis and hence the polarization along the x-axis vanishes.

The time variation depicted in Figure 4 reveals that the reaction of the electron states $|\Psi_\alpha\rangle$ on the applied vortex beam is on a sub-ps time scale as the polarization parameter starts to increase immediately for times $t > 0$. $\langle \cos \varphi \rangle (t > 0) > 0$ means that the electron states of the ring structure due to the light–matter interaction begin to orientate along the x-axis in direction of the clamped conductive straight channel. This could be explained by the directed flux of the charge density into the wire due to tunneling through the thin barrier region which has its origin by the increased effective centrifugal force. When the pulse is switched off (or has reached its peak amplitude), the electron states inside the ring structure start to loose their orientation which is accompanied by the decrease of the polarization parameter for propagation times $t > 1.7$ ps. This effect of the redistribution is

enhanced due to relaxation processes characterized by the relaxation time τ_{rel}. The small oscillations within the curve are related to the frequency of the transitions between the two levels around the Fermi energy which in turn are related to the round trip frequency in the ring.

3. Non-resonant transitions of the 2D hydrogen atom

Now we explore the possibility of observing the above effects for atomic systems and consider a 2D hydrogen atom in an intense laser field carrying OAM. Higher dimensions or many-electron atoms are still a challenge numerically. The current carrying states excited resonantly by circularly polarized plane waves were considered in Refs. (53). The focus here is on stimulated Raman-type excitations with OAM-carrying pulses in which case the light–matter coupling $\hat{H}_{Int}$ in Equation (1) differs markedly from the plane wave case. The vector potential of the linearly polarized ($\hat{\epsilon} = (1,0)^T$) OAM pulse is described by Eq. (2). The waist size of the beam in the x/y-plane is $w_0 = 50$ nm (945 a.u.) with the maximal intensity at the distance $w_0\sqrt{\ell_{OAM}/2}$ from the optical axis. A hydrogen atom at the vortex centre experiences so a very low intensity.

For numerical easiness, we employ a soft core Coulomb potential for the H atom:

$$V(r) = -\frac{1}{\sqrt{r^2 + a^2}}.$$

(7)

The cut-off parameter a is chosen in a way that the computed ground state energy is $E^{(1)} = -13.6$ eV. The electron states are characterized by the principal quantum numbers n and the angular quantum numbers m.

The amplitude of the vector potential A_0 is 0.5 a.u. at a radius $r = 2$ a.u., which means no tunnel ionization processes are expected. The photon energy $\hbar\omega = 4$ eV and therefore, no resonant transitions via single-photon processes will occur since the first unoccupied bound state in our H atom model lies at $E^{(2)} = -3.4$ eV. The temporal envelope of the field is modelled as $\Omega(t) = \exp[-(t - t_0)^2/t_s^2]$ where the parameter t_s is chosen in a way that the spectral width of the laser pulse is smaller than the energy difference $\Delta E = E^{(2)} - E^{(1)}$, i.e. $t_s = 20$ a.u. which corresponds to a FWHM of 806 as. As a consequence, all occurring optically induced transitions are due to second-order processes. The pulse is centred around at time t_0.

In the following, we consider the electron in the ground state characterized by quantum numbers $n = 1$ and $m = 0$ with the energy $E^{(1)}$ which is perturbed by the action of the laser pulse. The 2D-TDSE is solved full
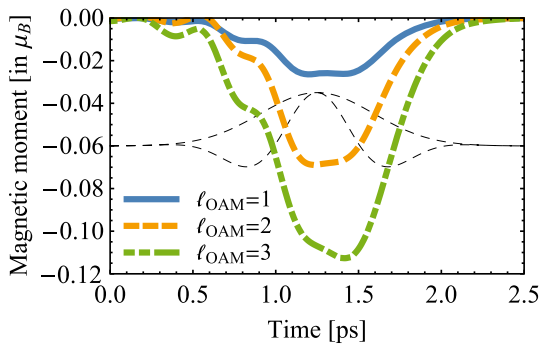
Figure 5. Magnetic moment in units of the Bohr magneton μ_B as a function of the propagation time for different topological charges ℓ_{OAM}. The FWHM of the temporal envelope of the applied OAM is 806 as while the peak intensity of the donut-shaped profile is 1.2×10^{18} W/cm^2. The black-dashed lines show the temporal variation of the applied OAM laser beam.

numerically from $t = 0$ to $t = 2.5$ ps. The centre of the pulse is characterized by $t_0 = 1.25$ ps.

In Figure 5 the magnetic moment in z-direction $m_z(t) = \int \mathrm{d}x \int \mathrm{d}y \, x j_y(x, y, t) - y j_x(x, y, t)$ in dependence on the topological charge of the vortex pulse is shown. Here, the vector $\boldsymbol{j}(\boldsymbol{r}, t) = (j_x(x, y, t), j_y(x, y, t))^T$ is the current density in the x/y-plane. The curves reveal that as long as the electric field is switched on, the magnetic moment increases which can be explained by non-resonant transitions due to second-order processes. Another important feature is the strong dependence on the topological charge ℓ_{OAM}. An increasing winding number leads to an increasing current density $\boldsymbol{j}(\boldsymbol{r}, t)$ and therefore, a larger magnetic moment. This can be explained by non-resonant transitions to states with higher angular quantum numbers m. The peaks of the depicted magnetic moments can be found around 1.25 ps propagation time which corresponds with t_0. When the pulse subsides, the magnetic moments decrease rapidly. The reason lies in the decreasing intensity of the laser pulse which lowers the probability for the second-order processes and non-resonant transitions. Therefore, the intensity profile of the applied OAM pulse is mapped into the temporal dependence of the photo-induced magnetic moments. We showed recently that the effect of transferring OAM to the electron is very sensitive to the position of the atom relative to the optical axis of the OAM laser spot (54). That means even for a distance between optical axis and atom on the atomic scale, the phase information carried by the OAM beam reduces drastically when translated to the atomic system. This issue is less critical for nano or microstructures (such as the rings presented here) which are conventionally etched or deposited on substrates. The possibility of near field vortex generation allows even to apply the field on a scale comparable or even less than the dimension of the microstructure.

4. Conclusions

We explored the potential of OAM-carrying laser pulses for generating unidirectional, non-equilibrium currents in nanoscale structures and atoms via stimulated Raman-type processes. Features of this type of current generation are distinctively different from direct resonant current generation. A main conclusion is that, short pulses are advantageous as the rise up time of the current as well as its magnitude are substantial. Longer pulses may be easier to handle theoretically, as they allow to employ a Floquet-type approach but higher peak intensities are needed and the current emerges much later, in which case relaxation processes may start to set in while the current is building up.

Disclosure statement

No potential conflict of interest was reported by the authors.

Funding

References

(1) Rosenfeld, L. On the Energy-momentum Tensor. *Mem. Acad. Roy. Belg.*, **1940**. 8(6), 1–30.

(2) Belinfante, F.J. On the Current and the Density of the Electric Charge, the Energy, the Linear Momentum and the Angular Momentum of Arbitrary Fields. *Physica* **1940,** *7,* 449–474.

(3) Cohen-Tannoudji, C.; Dupont-Roc, J.; Grynberg, G. Photons and Atoms. *Introduction to Quantum Electrodynamics*, Wiley: New York (NY), **1989**. Ch.1

(4) Soper, D.E. *Classical Field Theory*, Dover: New York (NY), **2008**. Ch.10.

(5) Allen, L.; Beijersbergen, M.W.; Spreeuw, R.J.C.; Woerdman, J.P. Orbital angular momentum of light and the transformation of laguerre-gaussian laser modes. *Phys. Rev. A* **1992,** *45,* 8185–8189.

(6) Beijersbergen, M.; Allen, L.; van der Veen, H.; Woerdman, J. Astigmatic Laser Mode Converters and Transfer of Orbital Angular Momentum. *Opt. Commun.* **1993,** *96,* 123–132.

(7) Beijersbergen, M.; Coerwinkel, R.; Kristensen, M.; Woerdman, J. Helical-wavefront Laser Beams Produced with a Spiral Phaseplate. *Opt. Commun.* **1994,** *112,* 321–327.

(8) He, H.; Friese, M.; Heckenberg, N.; Rubinsztein-Dunlop, H. Direct Observation of Transfer of Angular Momentum to Absorptive Particles from a Laser Beam with a Phase Singularity. *Phys. Rev. Lett.* **1995,** *75,* 826–829.

(9) Simpson, N.; Dholakia, K.; Allen, L.; Padgett, M. Mechanical Equivalence of Spin and Orbital Angular Momentum of Light: An Optical Spanner. *Opt. Lett.* **1997,** *22,* 52–54.

(10) Soskin, M.; Gorshkov, V.; Vasnetsov, M.; Malos, J.; Heckenberg, N. Topological Charge and Angular Momentum of Light Beams Carrying Optical Vortices. *Phys. Rev. A* **1997,** *56,* 4064–4075.

(11) Allen, L.; Barnett, S.M.; Padgett, M. *Optical Angular Momentum*; Institute of Physics Publishing, Bristol, **2003**.

(12) Molina-Terriza, G.; Torres, J.P.; Torner, L. Twisted Photons. *Nat. Phys.* **2007,** *3,* 305–310.

(13) Mair, A.; Vaziri, A.; Weihs, G.; Zeilinger, A. Entanglement of the Orbital Angular Momentum States of Photons. *Nature* **2001,** *412,* 313–316.

(14) Barreiro, J.T.; Wei, T.-C.; Kwiat, P.G. Beating the Channel Capacity Limit for Linear Photonic Superdense Coding. *Nat. Phys.* **2008,** *4,* 282–286.

(15) Boyd, R.W., et al. *Quantum Key Distribution in a High-dimensional State Space: Exploiting the Transverse Degree of Freedom of the Photon*, **2011**. *7948,* 79480L-1–79480L-6.

(16) Padgett, M.; Bowman, R. *Tweezers with a Twist. Nat. Phot.* **2011,** *5,* 343–348.

(17) Fürhapter, S.; Jesacher, A.; Bernet, S.; Ritsch-Marte, M. Spiral Interferometry. *Opt. Lett.* **2005,** *30,* 1953–1955.

(18) Woerdemann, M.; Alpmann, C.; Denz, C. Self-pumped Phase Conjugation of Light Beams Carrying Orbital Angular Momentum. *Opt. Expr.* **2009,** *17,* 22791–22799.

(19) Torres, J.P.; Torner, L. *Twisted Photons: Applications of Light with Orbital Angular Momentum*; Wiley-VCH, Weinsheim, **2011**.

(20) Andrews, D.L. *Structured Light and its Applications: An Introduction to Phase-structured Beams and Nanoscale Optical Forces*, Academic Press: **2011**.

(21) Foo, G.; Palacios, D.M.; Swartzlander, G.A. Jr; et al. Optical Vortex Coronagraph. *Opt. Lett.* **2005,** *30,* 3308–3310.

(22) He, H.; Heckenberg, N.; Rubinszstein-Dunlop, H. Optical Particle Trapping with Higher-order Doughnut Beams Produced Using High Efficiency Computer Generated Holograms. *J. Mod. Opt.* **1995,** *42,* 217–223.

(23) Wang, H.; Shi, L.; Lukyanchuk, B.; Sheppard, C.; Chong, C.T. Creation of a Needle of Longitudinally Polarized Light in Vacuum Using Binary Optics. *Nat. Phot.* **2008,** *2,* 501–505.

(24) Hell, S.W. Far-field Optical Nanoscopy. *Science* **2007,** *316,* 1153–1158.

(25) Allen, L. Introduction to the Atoms and Angular Momentum of Light Special Issue. *J. Opt. B: Quantum Semiclass. Opt*, **2002**. *4,* S1.

(26) Barreiro, S.; Tabosa, J. Generation of Light Carrying Orbital Angular Momentum via Induced Coherence Grating in Cold Atoms. *Phys. Rev. Lett.* **2003,** *90,* 133001.

(27) Friese, M.E.J.; Nieminen, T.A.; Heckenberg, N.R.; Rubinszstein-Dunlop, H. Optical Alignment and Spinning of Laser-trapped Microscopic Particles. *Nature* **1998,** *394,* 348–350.

(28) Romero, L.C.D.; Andrews, D.L.; Babiker, M. A Quantum Electrodynamics Framework for the Nonlinear Optics of Twisted Beams. *J. Opt. B: Quantum Semiclass. Opt.* **2002,** *4,* S66.

(29) Al-Awfi, S.; Babiker, M. Atomic Motion in Hollow Submicron Circular Cylinders. *Phys. Rev. A* **2000,** *61,* 033401.

(30) Araoka, F.; Verbiest, T.; Clays, K.; Persoons, A. Interactions of Twisted Light with Chiral Molecules: An Experimental Investigation. *Phys. Rev. A* **2005,** *71,* 055401.

(31) Helmerson, K.; Phillips, W.D. In Rotating atoms with light. *J. Torres, J. and L. Torner, L. (eds.) Twisted Photons: Applications of Light with Orbital Angular Momentum*, Wiley-VCH: Weinheim, **2011**. pp. 215–220.

(32) Quinteiro, G.F.; Berakdar, J. Electric Currents Induced by Twisted Light in Quantum Rings. *Opt. Expr.* **2009,** *17,* 20465.

(33) Wätzel, J.; Berakdar, J. Centrifugal Photovoltaic and Photogalvanic Effects Driven by Structured Light. *Sci. Rep.* **2016,** *6,* 21475.

(34) Quinteiro, G.F.; Tamborenea, P.I.; Berakdar, J. Orbital and Spin Dynamics of Intraband Electrons in Quantum Rings Driven by Twisted Light. *Opt. Expr.* **2011,** *19,* 26733.

(35) Noyan, M.A.; Kikkawa, J.M. Time-resolved Orbital Angular Momentum Spectroscopy. *Appl. Phys. Lett.* **2015,** *107,* 032406.

(36) Kirilyuk, A.; Kimel, A.V.; Rasing, T. Ultrafast Optical Manipulation of Magnetic Order. *Rev. Mod. Phys.* **2016,** *88,* 039904.

(37) Bose, T.; Berakdar, J. Nonlinear Magneto-optical Response to Light Carrying Orbital Angular Momentum. *J. Opt.*, **2014**. *16,* 125201.

(38) Koeksal, K.; Berakdar, J. Charge-current Generation in Atomic Systems Induced by Optical Vortices. *Phys. Rev. A* **2012,** *86,* 063812.

(39) Wätzel, J.; Pavlyukh, Y.; Schäffer, A.; Berakdar, J. Optical Vortex Driven Charge Current Loop and Optomagnetism in Fullerenes. *Carbon* **2016,** *99,* 439–443.

(40) Lévy, L.; Dolan, G.; Dunsmuir, J.; Bouchiat, H. Magnetization of Mesoscopic Copper Rings: Evidence for Persistent Currents. *Phys. Rev. Lett.* **1990,** *64,* 2074–2077.

(41) Mailly, D.; Chapelier, C.; Benoit, A. Experimental Observation of Persistent Currents in Gaas-algaas Single Loop. *Phys. Rev. Lett.* **1993,** *70,* 2020–2023.

(42) Fridkin, V. Bulk Photovoltaic Effect in Noncentrosymmetric Crystals. *Crystallogr. Rep.* **2001,** *46,* 654–658.

(43) Young, S.M.; Zheng, F.; Rappe, A.M. First-principles Calculation of the Bulk Photovoltaic Effect in Bismuth Ferrite. *Phys. Rev. Lett.* **2012,** *109,* 236601.

(44) Ziman, J.M. *Principles of the Theory of Solids*, 2nd ed.; Cambridge University Press, Cambridge, **1998**.

(45) Matos-Abiague, A.; Berakdar, J. Field-free Charge Polarization of Mesoscopic Rings. *Phys. Rev. B* **2004,** *70,* 195338.

(46) Moskalenko, A.S.; Matos-Abiague, A.; Berakdar, J. Revivals, Collapses, and Magnetic-pulse Generation in Quantum Rings. *Phys. Rev. B* **2006,** *74,* 161303.

(47) Haug, H. *and Jauho*; A.-P. Quantum Kinetics in Transport and Optics of Semiconductors, Springer, Berlin, **1996**.

(48) Matos-Abiague, A.; Berakdar, J. Photoinduced Charge Currents in Mesoscopic Rings. *Phys. Rev. Lett.* **2005,** *94,* 166801.

(49) Moskalenko, A.S.; Pavlyukh, Y.; Berakdar, J. Attosecond Tracking of Light Absorption and Refraction in Fullerenes. *Phys. Rev. A* **2012,** *86,* 013202.

(50) Dion, C.; Keller, A.; Atabek, O. Orienting Molecules Using Half-cycle Pulses. *EPJ D* **2001,** *14,* 249.

(51) Matos-Abiague, A.; Berakdar, J. Controlling the Orientation of Polar Molecules by Half-cycle Pulses. *Chem. Phys. Lett.* **2003**, *382,* 475–480.

(52) Matos-Abiague, A.; Berakdar, J. Sustainable Orientation of Polar Molecules Induced by Half-cycle Pulses. *Phys. Rev. A* **2003**, *68,* 063411.

(53) Barth, I.; Manz, J. Electric Ring Currents in Atomic Orbitals and Magnetic Fields Induced by Short Intense Circularly Polarized pi Laser Pulses. *Phys. Rev. A*, **2007**. *75,* 012510-1–012510-9. Quantum Switching of Magnetic Fields by Circularly Polarized Re-Optimized pi Laser Pulses: From One-Electron Atomic Ions to Molecules. In Yamanouchi, K., Bandrauk, A.D., Gerber, G., Eds., Progress in Ultrafast Intense Laser Science VI, Springer Series in Chemical Physics, Vol. 99; Springer: Berlin, 2010; pp. 21–44.

(54) Wätzel, J.; Berakdar, J. Discerning on a Sub-optical-wavelength the Attosecond Time Delays in Electron Emission from Magnetic Sublevels by Optical Vortices. *Phys. Rev. A* **2016**, *94,* 033414.